

# Compressibility Effects for the AGARD-B Model

---

**S. Tuling\*†, B. Vallabh\*\* and M.F. Morelli\*\*\***

† Corresponding author, Sean Tuling, P.O. Box 395, Pretoria, 0001, South Africa, Tel : +27128414893, Fax : +27123491156, E-mail : stuling@csir.co.za

\*Principal Engineer, CSIR, Meiring Naude Rd, Pretoria, South Africa

\*\* Engineer, CSIR, Meiring Naude Rd, Pretoria, South Africa

\*\*\* Research Group Leader, Experimental Aerodynamics, CSIR, Meiring Naude Rd, Pretoria, South Africa

## Abstract

A numerical study of the flow topologies over the 60° delta wing of the AGARD-B model at Mach 0.80 has revealed that vortex bursting occurs between 13°-15° angle of attack, while vortex separation occurs above 18°. These aerodynamic features have been identified as additional comparison criteria which need to be replicated for facilities using the model for calibration or inter-tunnel comparison purposes. The numerical simulations were performed using ANSYS Fluent V13, a structured mesh with near wall treatment and the Spalart-Allmaras and  $\kappa$ - $\omega$  SST turbulence models, and validated experimentally in a 5'x5' transonic facility. Other aspects not previously identified or studied are firstly a recovery shock between the primary and secondary vortex that exists only when vortex bursting occurs, and secondly the lack of a shock between the wing and vortex when the flow topology corresponds to the centreline shock region as observed in other studies.

## Nomenclature

AGARD	Advisory Group for Aeronautical Research and Development
b	Wing span, 0.6m
$\bar{c}$	Mean aerodynamic chord, 0.34641m
CFD	Computational Fluid Dynamics
CN	Body axes normal force, non-dimensionalised by $\frac{1}{2}\rho V^2 S$
Cm	Body axes pitching moment, non-dimensionalised by $\frac{1}{2}\rho V^2 S \bar{c}$
D	Diameter or calibre, m
mrc	Moment reference centre, mm
MSWT	Medium Speed Wind Tunnel
MP	Move-pause
KWSST	$\kappa$ - $\omega$ SST turbulence model
S	Reference area (gross wing area), 0.1558846m <sup>2</sup>
SA	Spalart-Allmaras turbulence model
V	Velocity, m/s

$\alpha$  Angle of attack, degrees  
 $\rho$  Air density, kg/m<sup>3</sup>

## Introduction

The AGARD-B model was originally designed as a supersonic wind tunnel calibration standard, but has also found use as a calibration standard in transonic facilities<sup>(1)</sup>. A number of publically available tests have been performed<sup>(1),(2)</sup> and continue to be performed on this configuration as a tunnel calibration standard<sup>(3)</sup>. The configuration has also been used to study boundary layer transition effects<sup>(4)</sup>.

The configuration is of practical interest and serves as a useful standard because it represents wings and bodies used in slender body configurations where low aspect ratio wings of order 0.5 to 4 with swept back leading edges (> 45°) are commonly employed. The configuration consists of a sharp nose circular body with planar 60° sweep triangular delta wings of 4% thickness with a biconvex profile.

Previous tests have been performed by the Medium Speed Wind Tunnel<sup>(5)</sup> (MSWT) and other facilities<sup>(1)</sup> but without any detailed flow field investigation of the flow topologies. Given the continued use of AGARD-B as a calibration standard for transonic wind tunnels (which includes the MSWT), insight into the previously unreported vortex bursting effect, and its effect on the global loads, is therefore desirable for the use of the AGARD-B configuration as a standard. The purpose of this paper is to elucidate some of these effects.

The flow regimes that manifest themselves for delta wings have been classified according to Mach number and angles of attack normal to the wing leading edge. The Stanbrook-Squire line<sup>(6)</sup> separates flows with attached leading edges and separated flow leading edges. The flow topologies of delta wings or cropped delta wings are dominated by a leading vortex angles of attack greater than what can be considered low. Six non-attached flow regions have been identified<sup>(7)(8)</sup>. In the region where the flow is separated at the leading edge, or where the Mach number normal to the leading edge is less than one and is the flow regime of interest in this paper, two regions exist<sup>(7)</sup>, namely the leading edge separation region which has a secondary attached vortex and the centreline shock region prevalent at higher angles of attack normal to the leading edge.

The primary region of interest in this paper is the lower angle of attack leading edge separation region with a secondary vortex. Riou *et al*<sup>(9)</sup> studied the centreline shock region and identified a complex lambda shock structure in the region of the secondary vortex rather than a simple normal shock.

Leading vortices are subject to vortex breakdown which is the predominant mechanism for the initial loss of lift at subsonic speeds. A large volume of work has been performed regarding the flow over delta and cropped delta wings, and the aspect of vortex breakdown has been studied intensively in the past including the interpretation of vortex breakdown<sup>(10)(11)</sup>.

The mechanisms and structure of vortex bursting have been studied intensively in the past. Two primary bursting modes have been identified for delta wings, namely the bubble and spiral modes<sup>(11)(12)(13)(14)</sup>. For tubes, four other low Reynolds number modes exist<sup>(15)</sup>.

The vortex breakdown boundaries are summarised Stallings<sup>(16)</sup>. For a 60° delta wing, which is the subject of this paper, at incompressible speeds vortex breakdown occurs at the trailing edge 15° and rapidly moves to 40% of the chord as the angle of attack is increased by a couple of degrees<sup>(17)(18)</sup>. The vortex bursting position reaches the apex when the angle of attack is 30°.

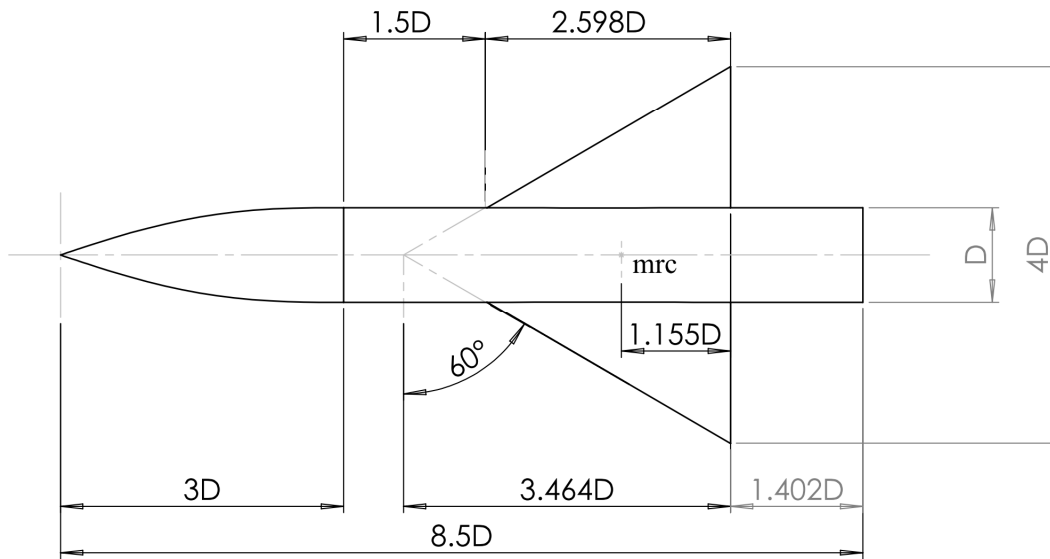
The unsteady or period flow aspects of vortex bursting have also been studied in the past including surface pressures, turbulence intensity, spectral density, frequency content and their effect on downstream surfaces<sup>(19)(20)(21)</sup>.

Vortex breakdown is of interest not only in its prediction due to detrimental effects, but also the ability to control or even enhance other desirable effects. Control of vortex breakdown has also been studied<sup>(22)(23)</sup> utilising control surfaces, blowing, suction, trailing edge jets and unsteady excitation.

## Numerical and Experimental Simulations

### Configuration

The AGARD-B configuration is an ogive constant diameter body with a 60° swept back biconvex triangular wing and is illustrated in Figure 1. The diameter of the body is 150mm.



Wing profile : symmetrical circular arc section. Thickness ratio = 0.04

Nose profile : length  $3D$ . Equation of curve  $r = \frac{x}{3} \left[ 1 - \frac{1}{9} \left( \frac{x}{D} \right)^2 + \frac{1}{54} \left( \frac{x}{D} \right)^3 \right]$

Radii of nose and wing leading edges should be  $D/500$

Figure 1. AGARD-B configuration and dimensions

## Experimental Tests

The vortex bursting effect manifests itself as a loss of lift or normal force at angles of attack greater than  $13^\circ$  for all subsonic Mach numbers, with the consequential change in pitching moment. The effect does not exist at the greater than Mach 1 transonic speeds because the flow over the wing is supersonic, which is consistent with the data obtained by Imai *et al*<sup>(24)</sup>.

Additional test were performed for this study to firstly confirm and then investigate the change in normal force and pitching moments between  $13^\circ$  and  $15^\circ$ . The tests by Lombardi *et al*<sup>(5)</sup> were performed in a move-pause testing mode with angle of attack increments of  $2.5^\circ$ , which is consistent with the data increments of the time. The experimental tests in this paper were performed in a continuous sweep mode to capture the vortex bursting effect on the global loads more effectively. The change in normal force as vortex bursting occurs in is shown in detail in Fig. 2, where the normal force for both data acquisition modes (move pause and continuous sweep) are shown. The drop in normal force is accompanied by an increase in the pitching moment indicating that the vortex bursting effect is aft of the moment reference centre (mrc). The move-pause mode is denoted by MP, whilst the continuous sweep mode is assumed to be the default mode. The experimental data shows that whilst the move-pause mode captures the effect, the move-pause increments do not expose the vortex bursting effect effectively. No attempt was made to determine whether

hysteresis exists, and all tests were performed with the angle of attack increasing as data were collected.

The tests were performed at a Mach number of 0.80 and a total pressure of 60kPa and total temperature of 315K, or Reynolds number of 1.125 million based on the body diameter of 150mm.

The estimated uncertainties (using a coverage factor of  $k=2$ ) in the angle of attack, normal force and pitching moment coefficients are  $0.08^\circ$ , 0.005 and 0.001 respectively.

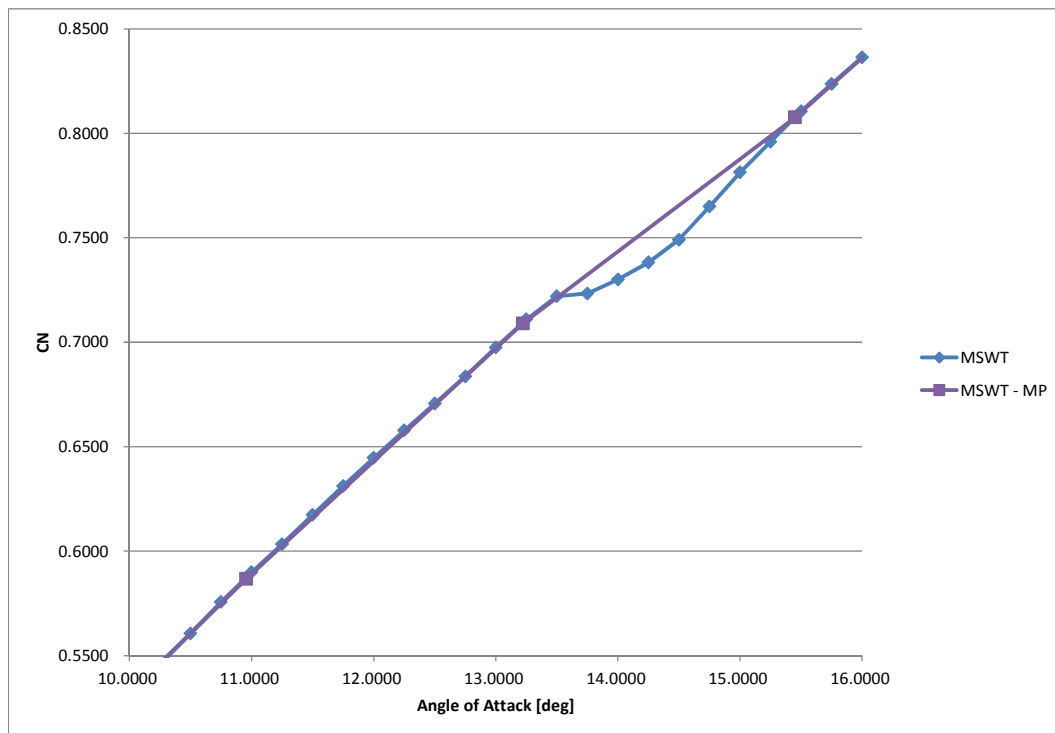


Figure 2. Vortex bursting effect on body-axes normal force (move pause is denoted by MP)

## Numerical Simulations

To study the flow phenomena causing this effect, steady state CFD simulations were performed. The simulations used the finite volume code ANSYS Fluent V13 with a second order upwind spatial discretisation scheme and second order  $\kappa$ - $\omega$  SST (KWSST) turbulence model utilising near wall treatment. A structured hexahedral mesh was used rather than tetrahedral cells. The boundary layer thickness was calculated using flat plate theory and at least 20 cells were used for the boundary layer. Furthermore, the  $y^+$  was checked to be of order 1 and less than 3. The structured mesh utilised 2.98million cells with the far field boundaries placed at least 20 body lengths away. The surface mesh geometry for the overall configuration, wing and base area are illustrated in Fig. 3. The inlet boundary condition was defined as a pressure inlet whilst the outlet boundary was defined as a pressure outlet. The total and static pressures; and total pressures used were the same as the experimental tests. The turbulence intensity was set to 0.1% and the length scale to  $10\mu\text{m}$ ; this also corresponding to the MSWT.

The solver used was the coupled-implicit density based formulation with the Roe convective flux-difference splitting scheme. Simulations were initialised using the built-in Full Algebraic Solver (FAS)

and run until the residuals of the primary variables dropped by at least three orders of magnitude and the loads asymptoted to constant values.

The study also investigated the use of the Spalart-Allmaras (SA) turbulence model because of its lower computational cost. The same mesh was utilised for this turbulence model as the  $\kappa\text{-}\omega$  SST turbulence model, also resulting in the same near wall boundary layer treatment. Only a half model was simulated because no asymmetric vortices from the wing or body manifest themselves at the angles of attack under consideration.

A mesh convergence study was conducted for both the  $\kappa\text{-}\omega$  SST and SA turbulence model. The study, which monitored the global loads, indicated that the mesh used was sufficiently refined.

The good correlation was obtained between the experimental and CFD simulations for the normal force and pitching moment, as illustrated in Fig. 4 and Fig. 5 over the angle of attack range of  $0^\circ$  to  $20^\circ$ . Three regimes of flow have been identified namely attached leading edge vortex ( $\alpha < 13^\circ$ ), vortex bursting ( $13^\circ \leq \alpha \leq 18^\circ$ ) and lastly vortex separation ( $\alpha > 18^\circ$ ).

The vortex bursting effect is less pronounced in the pitching moment. The CFD simulations utilising the different turbulence models both reproduce the vortex bursting effect, though the simulations of the  $\kappa\text{-}\omega$  SST correlate better than the SA turbulence model with regards to the angle of attack at which vortex bursting occurs, and is illustrated in Fig. 6 and Fig. 7. These figures plot the normal force and pitching moments of Fig. 4 and Fig. 5 for the limited angle of attack range of  $10^\circ$  to  $16^\circ$ . The SA turbulence model predicted vortex bursting occurring at a lower angle of attack ( $\sim 12.5^\circ$ ) than the  $\kappa\text{-}\omega$  SST model and experimental data ( $\sim 13.5^\circ$ ). The pitching moment for the  $\kappa\text{-}\omega$  SST model is predicted to be 0.02 of a caliber further aft than the experimental data and Spalart-Allmaras simulations. These differences notwithstanding, the CFD simulations predict the trends in the loads well and were therefore considered sufficiently validated to explore the flow field.

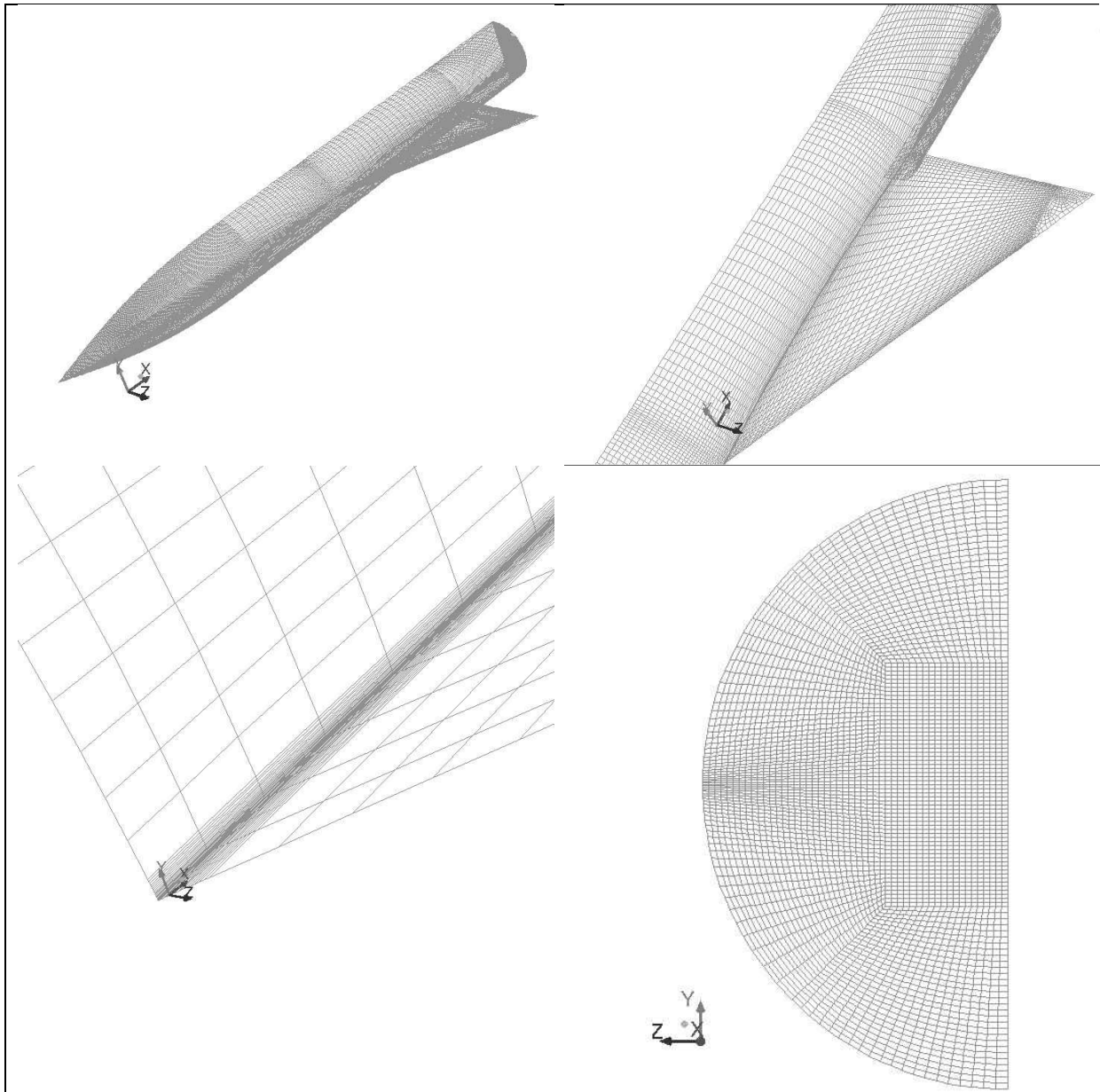


Figure 3. Surface mesh geometries for the overall configuration (top left), wing (top right), near wall boundary layer treatment (bottom left) and base area (bottom right)

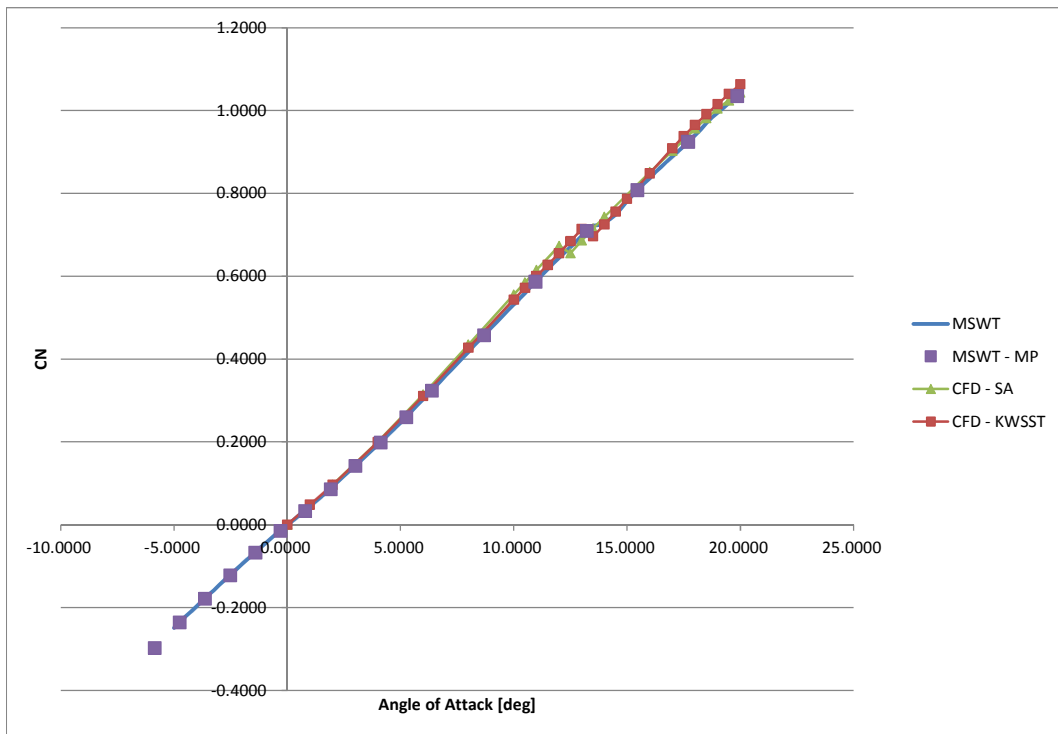


Figure 4. Normal force comparison between experimental tests and CFD simulations for the Spalart-Allmaras (SA) and  $\kappa$ - $\omega$  SST (KWSST) turbulence models

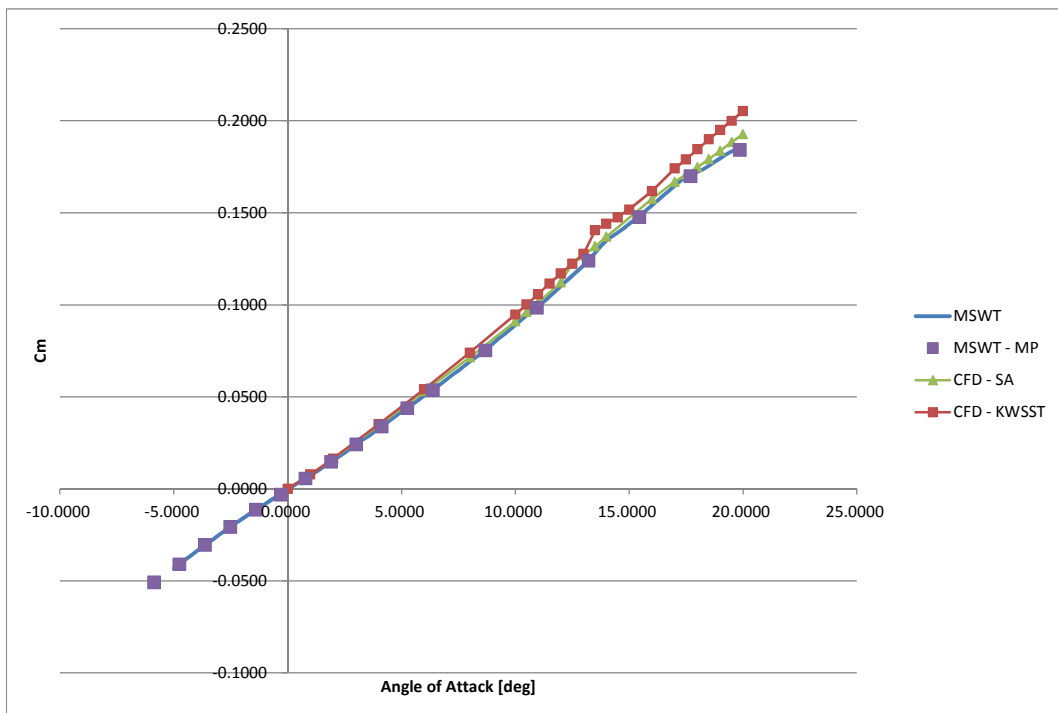


Figure 5. Pitching moment comparison between experimental tests and CFD simulations for the Spalart-Allmaras (SA) and  $\kappa$ - $\omega$  SST (KWSST) turbulence models



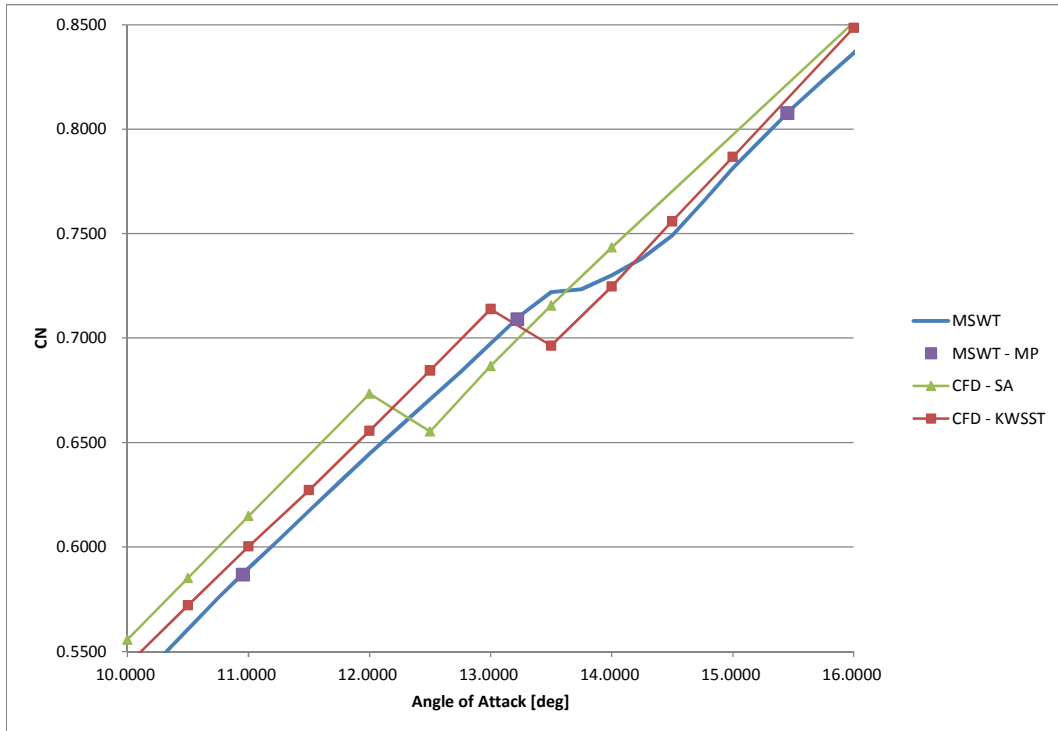


Figure 6. Vortex bursting effect on normal force comparison between experimental tests and CFD simulations for the Spalart-Allmaras (SA) and  $\kappa$ - $\omega$  SST (KWSST) turbulence models over the limited angle of attack range of  $10^\circ$  to  $16^\circ$

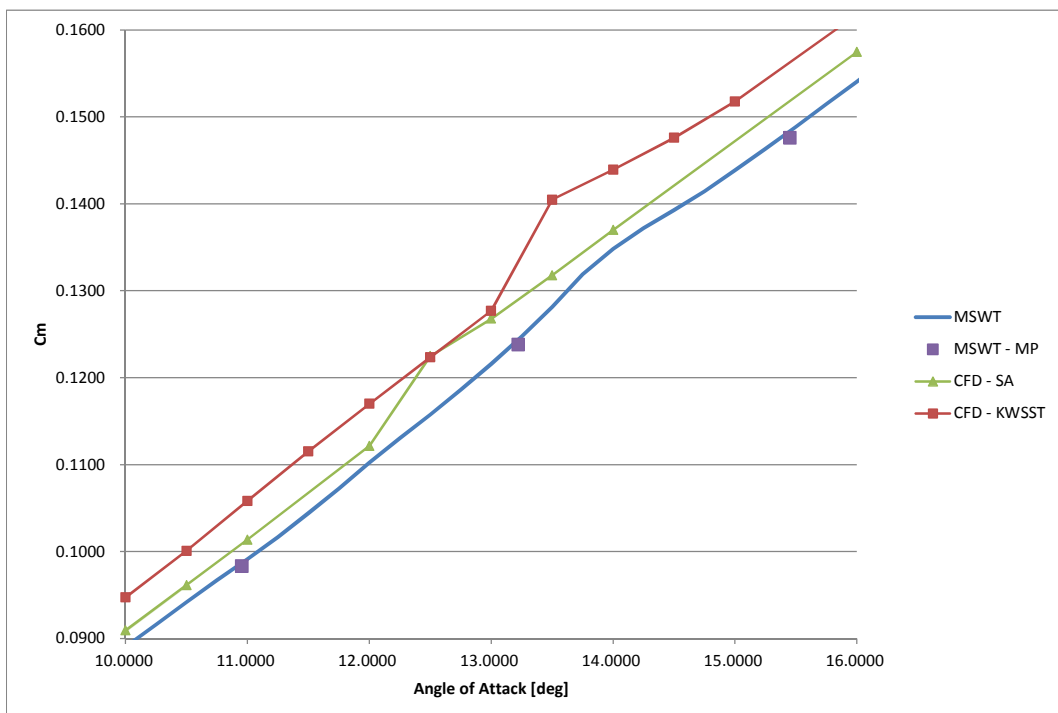


Figure 7. Vortex bursting effect on pitching moment comparison between experimental tests and CFD simulations for the Spalart-Allmaras (SA) and  $\kappa$ - $\omega$  SST (KWSST) turbulence models over the limited angle of attack range of  $10^\circ$  to  $16^\circ$

## Flow Field Observations

Comparisons between the CFD simulations between the two turbulence models revealed no significant differences in the flow structures and particularly with regards to the topology of the vortex when vortex bursting occurs. Given that the  $\kappa$ - $\omega$  SST turbulence model predicted the onset of vortex bursting with angle of attack better than the Spalart-Allmaras model even though the global loads correlate marginally less well, these simulations were used for subsequent analysis.

The global flow structures present on the AGARD-B model are the body vortices, the two secondary vortices at the wing body junction and the primary and secondary leading edges vortices. This is illustrated in Fig. 8 for an angle of attack of  $10^\circ$  at 6.667 calibers from the nose. The vortices are outlined by the  $\lambda_2$ -criterion as contours (from  $-1E7$  to  $-1E6$ ).

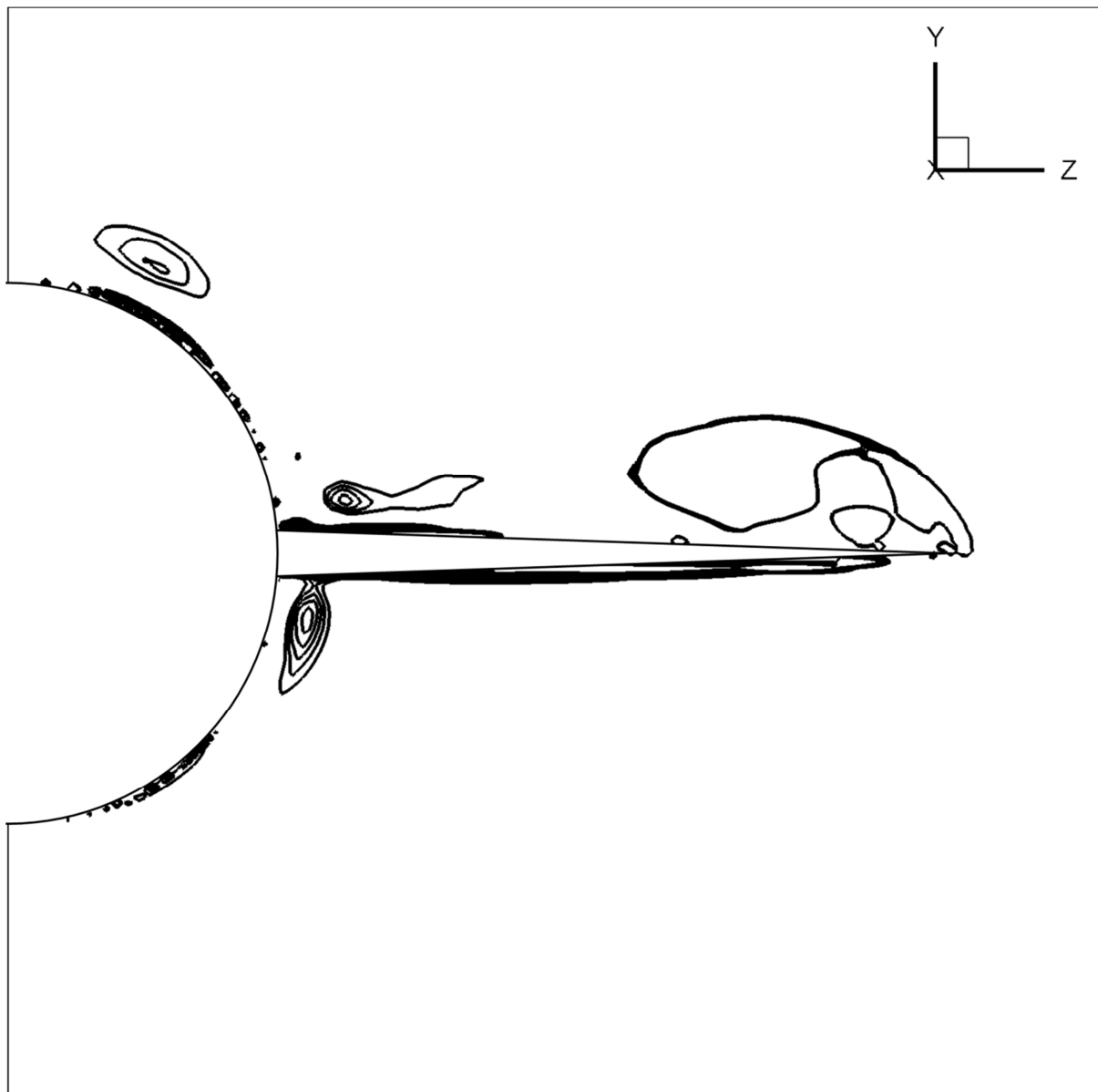


Figure 8. Primary vortex structures for  $\alpha=10^\circ$  at 6.667 calibers as contoured by the  $\lambda_2$ -criterion (values from  $-1E7$  to  $-1E6$ )

The CFD simulations correlate with the experimental tests where vortex bursting occurs at angles of attack above  $13^\circ$ , with the corresponding loss of lift for the configuration. The angle of attack at which this occurs is marginally lower than that for subsonic experiments for  $60^\circ$  delta wing configurations<sup>(17)</sup> and other investigations<sup>(24)</sup>. This is due to the effect of the body ("Beskin" upwash) increasing the local angle of attack of the wing.

As the angle of attack increases the vortex bursting location moves forward as expected. The vortex burst location at an angle of attack of  $20^\circ$  is at 5 calibers, or almost the apex of the exposed wing. This angle of attack is lower than the  $30^\circ$  predicted by Wentz<sup>(17)</sup> and is due to the increased local angle of attack due to the upwash of the body.

In contrast to Riou *et al*<sup>(9)</sup> and Kalkhoran *et al*<sup>(25)</sup>, the vortex breakdown is not triggered by a streamwise normal shock because no such shock exists for this configuration. Given that vortex breakdown occurs at similar angles for low speeds<sup>(17)</sup> and transonic speeds, the cause for the vortex breakdown has been attributed to the adverse pressure gradient of the flow over the circular arc profile. Similar to Riou *et al*<sup>(9)</sup> is the "kidney" shaped vortex rather than the circular vortex of incompressible speeds.

At the higher angles of attack ( $>16^\circ$ ), which corresponds to the centreline shock region for delta wings, no shock structures exist before vortex bursting occurs which is distinctly different to that observed by Riou *et al*<sup>(9)</sup>, where a lambda shock structure was identified between the primary vortex and the wing surface. The flow near the body experiences a higher angle of attack due to the upwash effect resulting in the normalised angle of attack. Also, no shocks exist on the upper side of vortex as identified by Riou *et al*<sup>(9)</sup> even though the flow over the top of the vortex sheet and vortex exceeds the speed of sound. This is illustrated in Fig. 9 for the angle of attack of  $17^\circ$ . Inspection of the flow between the primary vortex and the wing shows that the flow accelerates as it is entrained between the primary vortex and wing surface and decelerates isentropically as it flows between primary and secondary vortex.

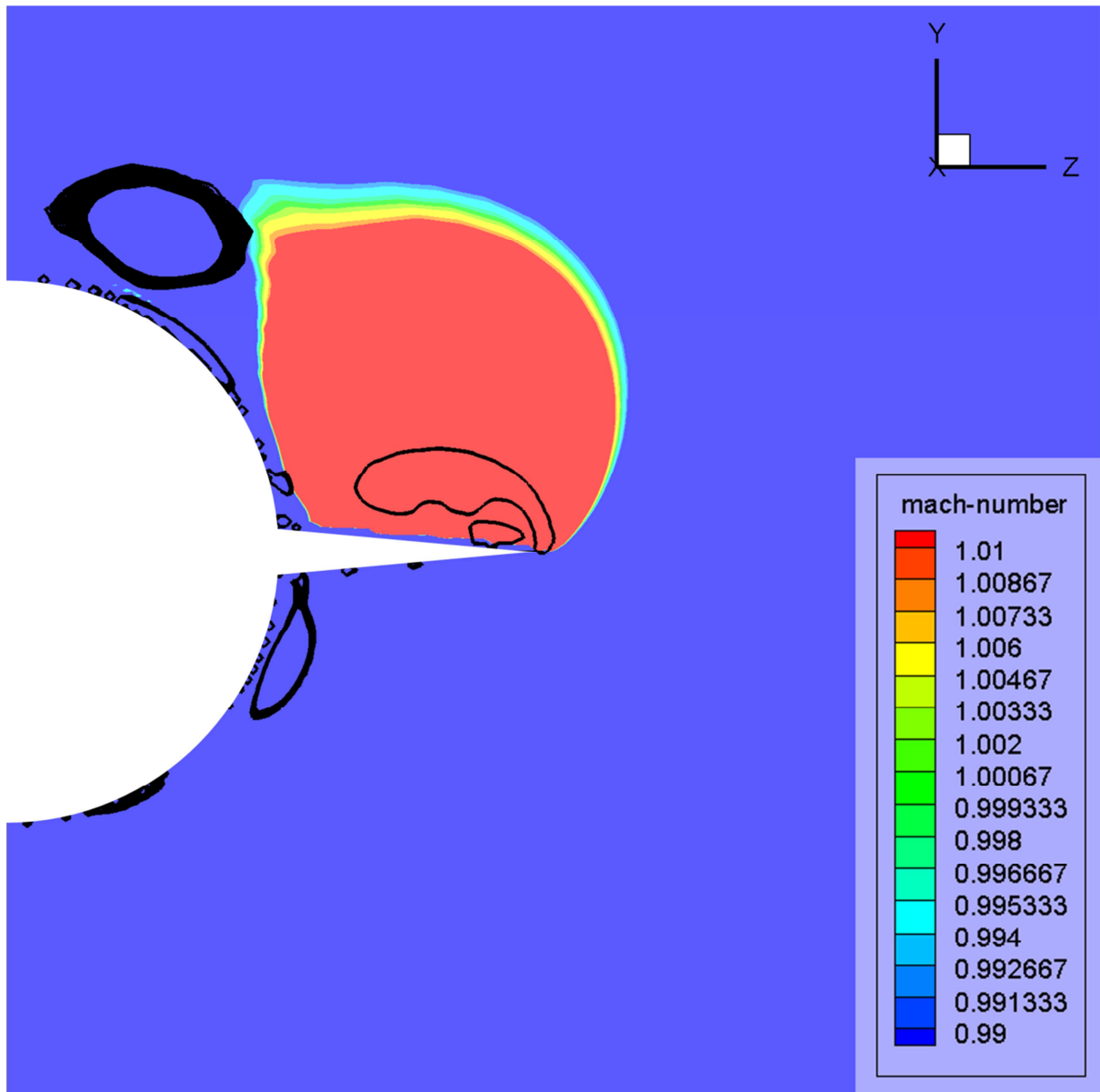


Figure 9. Mach number plot illustrating the lack of shock structures for  $\alpha=17^\circ$  at 5.333D

Inspection of the flow topology when vortex bursting occurs reveals a recovery shock between the primary and secondary vortices. This shock manifests itself as the flow, which is supersonic between the primary vortex and wing surface, decelerates over the secondary vortex. This is illustrated in Fig. 10, which shows contours of Mach number at a location of 6.333 calibers from the nose. Whilst it is more traditional to use density gradients to identify or highlight shock structures, the Mach contours illustrate the recovery shock better than the density gradients. The presence of the shock was corroborated by correlation of high density gradients with the sonic contour. The recovery shock only exists as the vortex is bursting and disappears once the vortex has fully burst because the flow between the burst vortex and wing surface does not exceed Mach 1.2 and the flow decelerates isentropically. This is illustrated in Fig. 11.

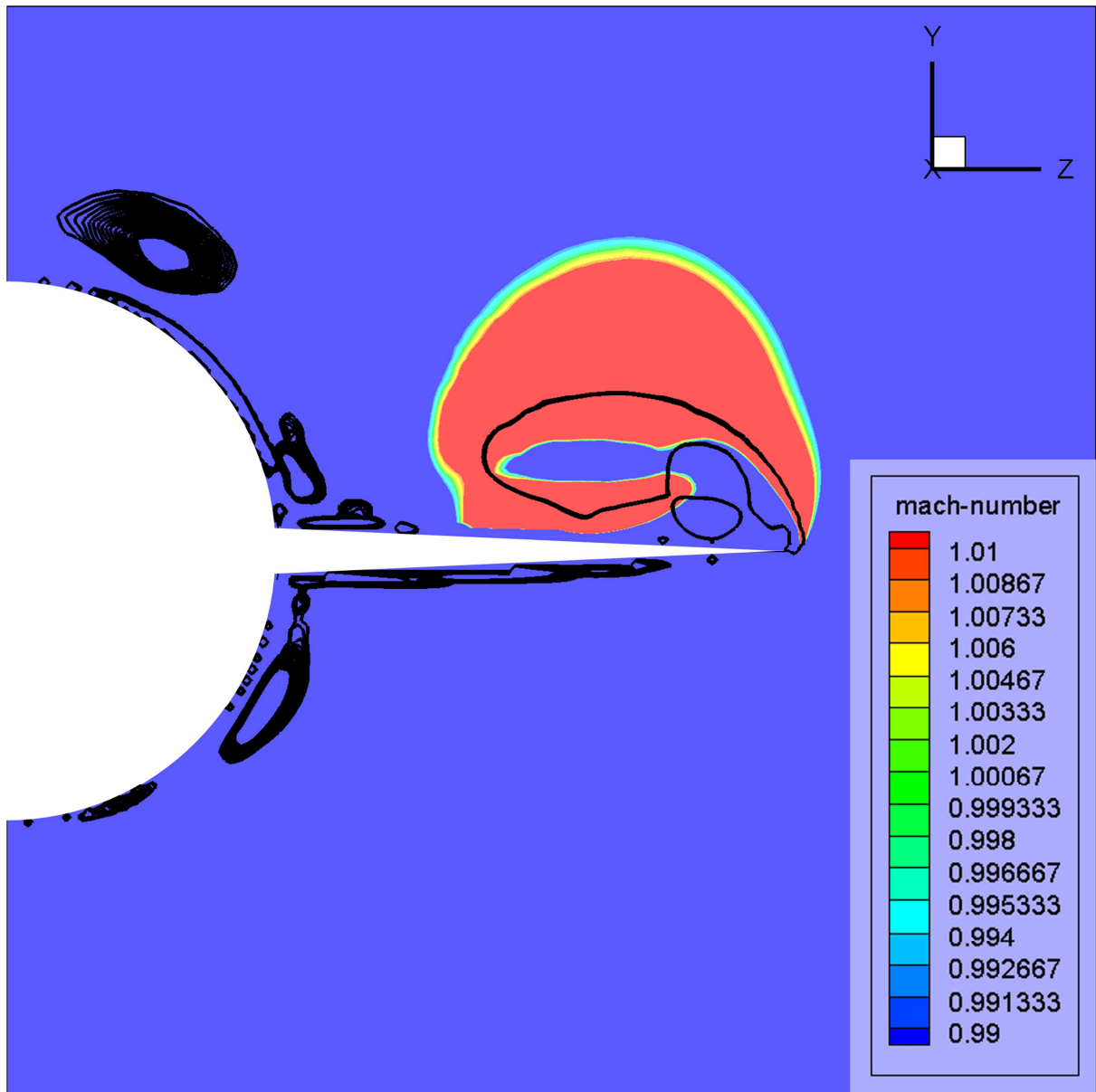


Figure 10. Recovery shock between the primary and secondary vortices for  $\alpha=14^\circ$  at station 6.133D

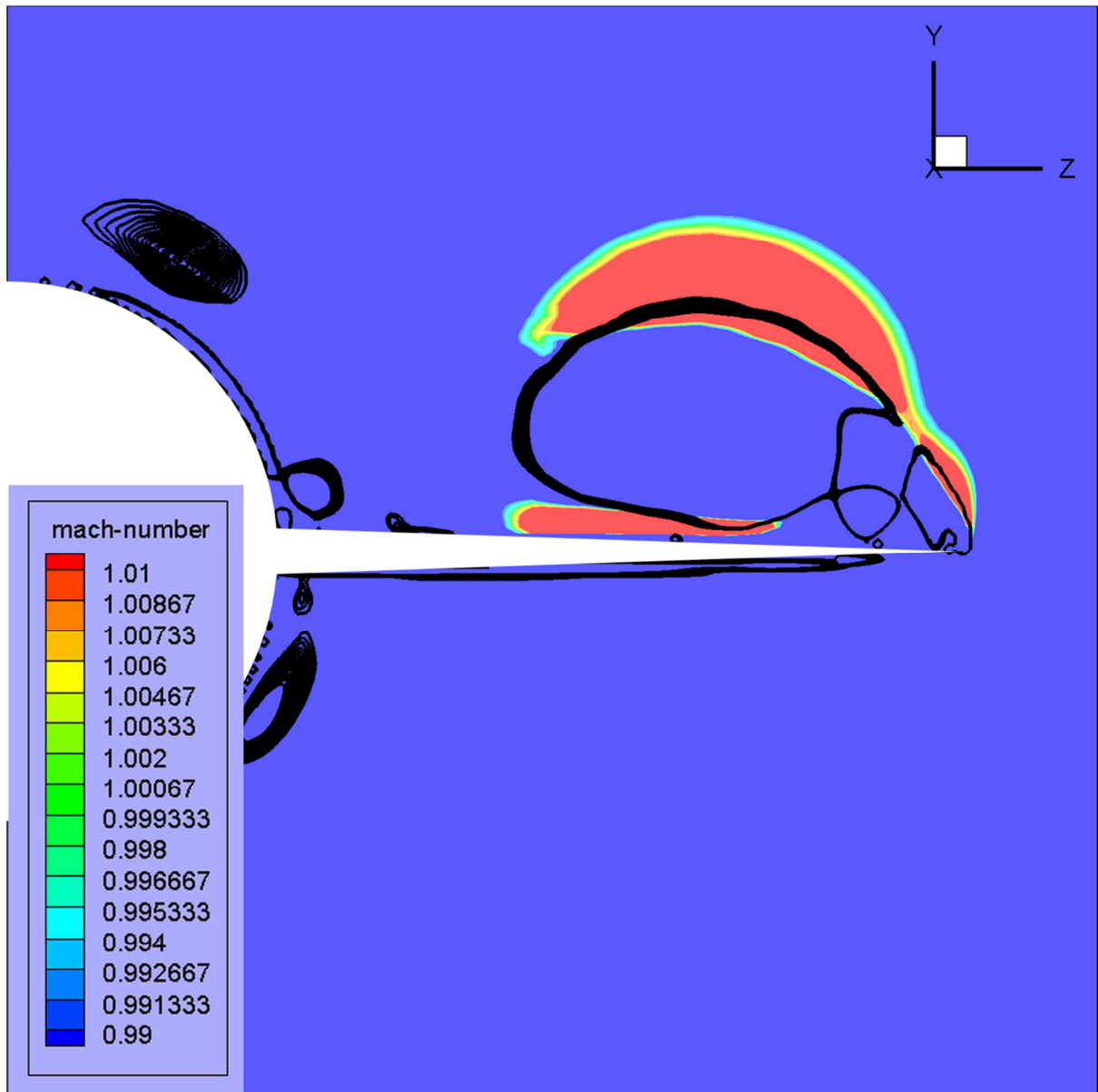


Figure 11. Mach contours for the fully developed vortex burst ( $\alpha=14^\circ$ , station 6.667 calibers)

Lastly, the reduction in normal force at angle of attack above  $18^\circ$  is due to the burst vortex separating or shedding from the wing. This is shown in Fig. 12 where simulated oil streamlines show the 'whorl' at the tip for the angle of attack of  $18.5^\circ$ .

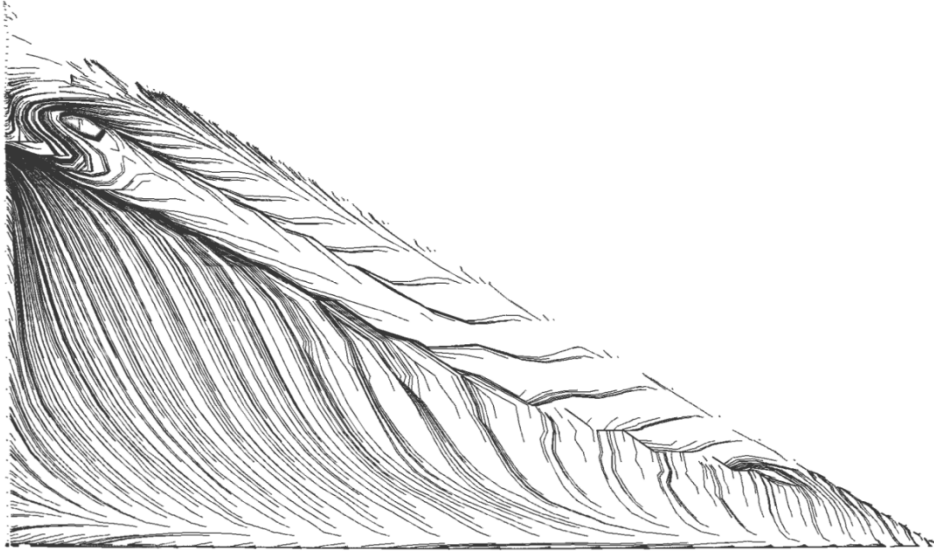


Figure 12. On-surface streamlines for  $\alpha=18.5^\circ$

The  $60^\circ$  biconvex AGARD-B wing only develops shock structures when the vortex bursts. At angles of attack greater than  $16^\circ$ , the normalised angle of attack and Mach number correspond to the centreline shock region of the established flow regimes<sup>(7)(8)</sup>. In this region a normal or lambda shock should exist between the primary vortex and the wing as the flow is initially accelerated and then decelerated to match the flow conditions between the secondary vortex and the vortex sheet or leading edge shear layer. Additionally, the cross flow shocks observed on the upper side of the primary vortex by Riou *et al* is not present for this configuration. The flow structures observed in previous studies are therefore not observed in this study and indicates that the geometry has a significant effect on the shock structures.

The changes in behaviour of the flow over the wing over the angle of attack range chosen provide a useful standard against which tunnels can be calibrated, especially because a number of non-linear planform/geometry driven phenomena are observed for this configuration. Publically available data presented in the past do not illustrate the effects where vortex bursting and vortex separation occur either because the data are not available or have not been analysed. Wind tunnels using this configuration as a standard would therefore need to demonstrate the capturing of both these phenomena.

## Conclusions

In conclusion, the following aspects not previously identified nor studied have been identified for the AGARD-B configuration at Mach 0.8. These are:-

- Vortex bursting between an angle of attack of  $13^\circ$  and  $15^\circ$  and vortex separation above angles of attack of  $18^\circ$

- Replication of the vortex bursting and vortex separation as additional comparison criteria if the configuration is to be used a tunnel calibration standard or for inter-tunnel calibration purposes
- As vortex bursting occurs a recovery shock that exists between the primary and secondary vortex
- When the flow corresponds to the centreline shock region, no shock exists between the vortex and wing surface which departs from the established flow classifications for sharp edged delta wings

## References

1. Hills, R., A Review of Measurements on AGARD Calibration Models, AGARDograph 64, November 1961
2. Anderson, C.F., An Investigation of the Aerodynamic Characteristics of the AGARD Model B for Mach Numbers from 0.2 to 1.0, AEDC-TR-70-100, Arnold Engineering Development Centre, Arnold AFB, Tennessee, May 1970
3. Damljanovic, D., Vitic, A. and Vukovic, D., Testing of AGARD-B calibration model in the T-38 trisonic wind tunnel, *Scientific Technical Review*, Vol LVI, No. 2, 2006
4. Ren Xudong, Gao, C., Zhao Zijie, Xiong Juntao, Liu Feng, Luo Shijun, Boundary-Layer Transition Effects on Aerodynamic Characteristics of AGARD-B Model, 50th AIAA Aerospace Sciences Meeting, see also, AIAA-2012-1217, DOI: 10.2514/6.2012-1217
5. Lombardi, G. and Morelli, M.F.M., Analysis of Some Interference Effects in a Transonic Wind Tunnel, *Journal of Aircraft*, Vol 32, No. 3, May-June 1995.
6. Stanbrook, A. and Squire, L.C., Possible Types of Flow at Swept Leading Edges, *Aeronautical Quarterly*, Vol. XV, 1964, pp. 72-82
7. Szodruch, J.G. and Peake, D.J., Leeward Flow Over Delta Wings at Supersonic Speeds, NASA-TM-81187, April 1980.
8. Miller, D.S. and Wood, R.M., An Investigation of Wing Leading-Edge Vortices at Supersonic Speeds, AIAA Paper 83-1816, July 1983.
9. Riou, J., Garnier, E. and Basdevant, C., Compressibility effects on the vortical flow over a 65° sweep delta wing, *Physics of Fluids*, 22 (10), 2010, DOI : 10.1063/1.3327286
10. Keller, J.J., On the interpretation of vortex breakdown, *Physics of Fluids*, 7(7), July 1995
11. Hall, M.G., Vortex Breakdown, *Annual Review of Fluid Mechanics*, Vol. 4, pp. 195-218, 1972
12. Delery, J.M., Aspects of Vortex Breakdown, *Progress in Aerospace Sciences*, Vol 30, pp. 1-59, 1994
13. Esducier, M., Vortex Breakdown : Observations and Explanations, , *Progress in Aerospace Sciences*, Vol. 25, pp. 189-229, 1988
14. Calderon, D. E., Wang, Z. and Gursul, I. Three-dimensional measurements of vortex breakdown. *Experiments in Fluids*, 53(1), 2012, pp. 293-299
15. Lucca-Negro, O. and O'Doherty, T., Vortex breakdown : a review, *Progress in Energy and Combustion Science*, Vol. 27, pp 431-481, 2001
16. Stallings, R.L., Low Aspect Ratio Wings at High Angles of Attack, Tactical Missile Aerodynamics, Progress in Astronautics and Aeronautics, American Institute of Aeronautics and Astronautics, 1986



17. Wentz, W.H. and Kohlman, D.L. Vortex Breakdown on Slender Sharp-Edged Wings, *Journal of Aircraft*, Vol 8, No 3, pp-156-161, March 1971.
18. Earnshaw, P.B. and Lawford, J.A., Low-Speed Wind-Tunnel Experiments on a Series of Sharp-Edged Delta Wings, Aeronautical Research Council R. & M. No. 3424, 1966.
19. Gursul, I., Review of Unsteady Vortex Flows over Slender Delta Wings, *Journal of Aircraft*, Vol. 42, No.2, March-April 2005
20. Ismet Gursul. "Unsteady flow phenomena over delta wings at high angle of attack", *AIAA Journal*, Vol. 32, No. 2 (1994), pp. 225-231. doi: 10.2514/3.11976
21. Breitsamter, C., Unsteady flow phenomena associated with leading-edge vortices, *Progress in Aerospace Sciences*, Vol 44, pp. 48-65, 2008
22. Mitchell, A.M. and Delery, J., Research into vortex breakdown control, *Progress in Aerospace Sciences*, Vol 37, pp. 385-418, 2001
23. Gursul, I., Wang, Z. and Vardaki, E., Review of flow control mechanisms of leading-edge vortices, *Progress in Aerospace Sciences*, Vol 43, pp. 246-270, 2007
24. Imai, G., Fuji, K. and Oyama, A., Computational Analyses of Supersonic Flows Over a Delta Wing at High Angles of Attack, 25<sup>th</sup> International Congress of the Aeronautical Sciences, 3-8 September 2006, Hamburg, Germany
25. Kalkhoran, I.M. and Smart, M.K., Aspects of shock wave-induced vortex breakdown, *Progress in Aerospace Sciences*, Vol 36, pp. 63-95, 2000